

# Directional Fractal Signature Analysis of Self-Structured Surface Textures

Marcin Wolski · Pawel Podsiadlo · Gwidon W. Stachowiak

Received: 10 April 2012 / Accepted: 18 May 2012 / Published online: 8 June 2012  
 © Springer Science+Business Media, LLC 2012

**Abstract** Currently available directional fractal signature (DFS) methods are not suited for self-structured surface textures since they base on the assumption of Brownian fractal or they do not use the entire image data in calculation. To address these difficulties, two new DFS methods were developed in this study, i.e., an augmented blanket with rotating grid (ABRG) method and a blanket with shearing image (BSI) method. The performance of these methods in measuring surface roughness and directionality, the capacity for quantifying multi-patterned textures, and the ability to detect differences between textures of self-structured surfaces were evaluated. The methods were compared against a blanket with rotating grid (BRG) method. Computer-generated images of self-structured surface textures with different roughness, directions and patterns, and atomic force microscope images of real self-structured surfaces were used. The computer texture images were generated using a specially developed motif-based texture generator. Results obtained showed that the ABRG method is more accurate and reliable than the BRG and BSI methods.

**Keywords** Surface characterization · Self-structured surfaces · Numerical analysis · Texture

## List of symbols

$a_1, a_2$                       Scaling factors  
 $A$                                 Surface area

$d_m$                               Size of structuring element (pixel)  
 $FD$                                 Fractal dimension  
 $i, j$                                 Indices of a motif coordinates  
 $I, I_r$                               Images  
 $\mathbf{K}_n$                                 Matrix used for dilation and erosion  
 $L_x, L_y$                           Spatial domains  
 $L_z$                                 Gray-scale level domain  
 $m, n$                               Indices of structuring element size and direction  
 $m_h$                                 Surface height of a motif (gray-scale level value)  
 $N_x, N_y, N_r, N_g, N_h$         Image and matrix dimensions  
 $N_d, N_\theta$                         Number of structuring element sizes and directions  
 $N_z$                                 Number of gray-scale level values  
 $r_1, r_2, r_3$                       Ellipsoid radii ( $r_1, r_2$ —pixel;  $r_3$ —gray-scale level value)  
 $s_x, s_y$                           Distances between centers of motifs (pixel)  
 $S$                                   Slope of line fitted at individual scale  
 $S_a$                                 3D average roughness ( $\mu\text{m}$ )  
 $V$                                   Volume enclosed between dilated and eroded images  
 $x, y$                                 Image coordinates  
 $x_c, y_c$                           Coordinates of a pixel used for cropping  $I_r$   
 $x_i, y_j, x', y', x'', y'', x_r, y_r$     Coordinates of a motif in  $I_r$   
 $x_1, y_1$                               Local coordinates within a motif  
 $z$                                   Gray-scale level value  
 $\alpha$                                 Orientation of ellipsoid ( $^\circ$ )

M. Wolski (✉) · P. Podsiadlo · G. W. Stachowiak  
 Tribology Laboratory, School of Mechanical and Chemical Engineering, The University of Western Australia, 35 Stirling Highway, Crawley, WA 6009, Australia  
 e-mail: marcin@mech.uwa.edu.au

$\beta$	Rotation angle ( $^{\circ}$ )
$\theta_n$	Direction of FDs calculations ( $^{\circ}$ )

## 1 Introduction

Self-structured surface textures gained an increasing interest over last decades as means for improving wear resistance and reducing friction in microsize devices (micromotors or microgrippers) [1, 2], controlling adhesion at interfaces [3, 4], reducing corrosion [5], and designing new biosensors or coatings [6, 7]. The surface textures are generated according to self-assembling rules of molecules of organic or chemical compounds that bond to a base surface by a complicated and not yet fully understood process [8]. The results of this assembling process are surface textures that have topographical features (motifs) of various sizes, shapes, and orientations, recurring at different locations and scales in one or more layers (Fig. 1).

Owing to the complex nature of self-structured surfaces, visual examination is the method of choice in their evaluation. This was done by optical [2], scanning electron (SEM) [9], scanning tunneling (STM) [10], Fourier transform infrared spectroscopy (FTIS) [4] or atomic force (AFM) microscopes [2, 10–12]. Several attempts were made for numerical characterization of self-structured surface texture images, including Fourier transform [13, 14], root-mean-square (RMS) roughness [1, 9], and average height of surface profiles methods [15]. Fractal analysis was also attempted, e.g., by box-counting [16] or slit-island methods [17]. However, these methods have limited use as they do not quantify surface textures at different scales and directions. This could be overcome by directional fractal signature (DFS) methods.

DFS methods are able to calculate fractal dimensions (FDs) at individual scales [i.e., fractal signature (FS)] in

different directions. Currently, three methods have this unique ability, i.e., FS Hurst orientation transform (FSHOT) method, variance orientation transform (VOT) method, and blanket with rotating grid (BRG) method [18]. The FSHOT and VOT methods are based on statistical properties of gray-scale level differences and they calculate maximum values or variances (standard deviations) of those differences at different scales and directions. The third method is based on dilations and erosions of image data with horizontal line structuring elements (SEs) and it calculates surface areas at different scales for different directions. The FSHOT and VOT methods require image data to be Brownian fractal. The accuracy of these three methods was evaluated using computer generated fractal surfaces and images of trabecular bone texture [18]. The VOT method showed the best performance. Also, further studies showed that the VOT method is an accurate tool for the detection and prediction of knee osteoarthritis [19, 20]; it can detect minute differences between ground and sandblasted surfaces, and between surfaces of adhesive wear particles generated under different operating conditions [21]. However, the VOT method is not suitable for the characterization of self-structured surfaces since they are not Brownian fractals (discussed in next section). The BRG method appears as a good choice. However, the rotating grid in the method is smaller than the image size, and, subsequently, some image data are not used in calculations of FSs.

To address this problem, in this paper, two new methods are developed, i.e., an augmented blanket with rotating grid (ABRG) method and a blanket with shearing image (BSI) method. Both methods are based on dilations and erosions of image data performed with horizontal line SEs. Unlike the BRG method, the ABRG method has the size of the rotating grid that is automatically adjusted for each direction to insure that entire image data is used. In the BSI method, the rotating grid is not employed. Instead, the dilations and erosions are performed on skewed images

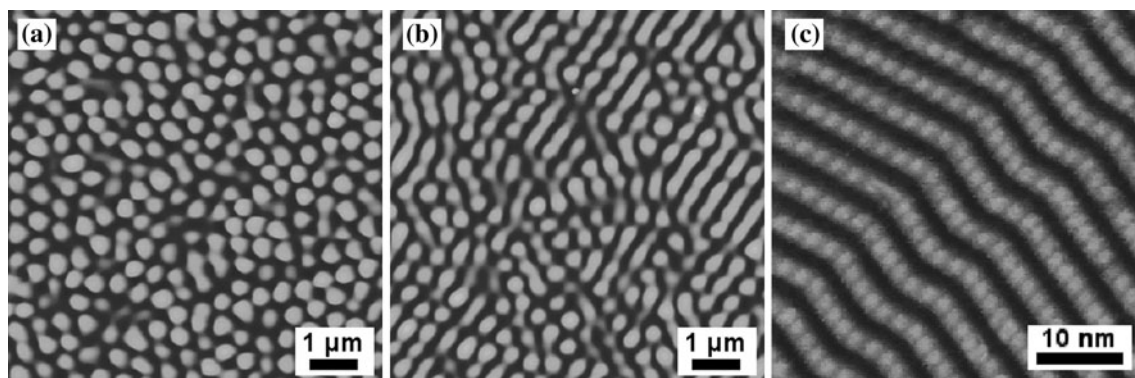


**Fig. 1** AFM images of self-structured surfaces photoinduced with **a** circularly and **b** linearly polarized laser beams (adapted from [13]), and **c** STM image of twofold symmetrical surface (adapted from [11]). The surfaces are not Brownian fractals

obtained by shearing the original image along its border over calculated distances. The performance of the methods in measuring surface roughness and directionality, and their capacity for quantifying multi-patterned textures were evaluated. For this purpose, computer images of self-structured surface textures with different roughness, directions, and patterns were used. A motif-based texture generator (MTG) was developed to generate the images. Also, the methods were evaluated for detection of differences between self-structured surfaces produced with circularly and linearly polarized laser beams.

## 2 Brownian Fractal Surfaces

Surface image is Brownian fractal if it has the two following properties [22]:

1. the distribution of gray-scale level differences calculated at different pixel distances (i.e., scales) in each direction is approximately normal, and
2. a line can be accurately fitted to a log–log plot of variances (or standard deviations) of gray-scale level differences against pixel distances.

Examples of non-Brownian and Brownian fractal surface images are shown in Figs. 1a, c, and 2. They are AFM and STM images of self-structured surfaces (Fig. 1a, c) and a SEM image of an adhesive wear particle surface (Fig. 2). The self-structured surfaces were obtained through irradiation of an azo polymer film with a circularly polarized laser beam [13] (Fig. 1a) and through varying lengths of alkyl-substituted phthalocyanines chains on graphite [11] (Fig. 1c). The wear particle was generated using a tribotester with stainless steel pin and mild steel disk under a load of 49.24 N and with sliding time of 180 s [21].

For the surface images, gray-scale level differences were calculated at different pixel distances and directions.

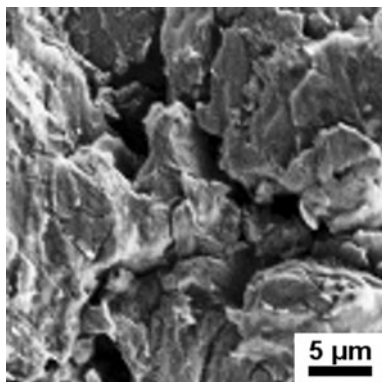


**Fig. 2** SEM image of an adhesive wear particle surface. The surface is Brownian fractal

The pixel distances were ranking from 4 to 16 pixel in steps of 1 pixel and directions from 0° to 180° in steps of 10°. For other directions, the differences were same because data are symmetric about the center of the image. A quantile–quantile (QQ) plot was constructed for each scale and direction. These plots compare values of gray-scale level differences with their expected normal values. When the values of the differences are normally distributed, the data points on the plot would follow a straight line. Also, for each direction, log–log plots of variances of the differences against distances were constructed. Examples of QQ plots obtained for the surface images in the horizontal and vertical directions at 10 and 13 pixel distances respectively are shown in Fig. 3. The corresponding log–log plots are also shown in Fig. 3. For the wear particle, data points on QQ and log–log plots follow a straight line with a good accuracy (Fig. 2a–d). This implies that the particle surface is Brownian fractal. In contrast, data points on QQ plots obtained for the self-structured surfaces exhibit “S-shape” (Fig. 3e, f, i, j) or “L-shape” (Fig. 3g, h, k, l) curve. These findings indicate that the two surfaces are non-Brownian fractal.

## 3 Methods and Materials

### 3.1 Directional Signature Methods

The BRG method is introduced first; followed by descriptions of the BRG and BSI methods.

#### 3.1.1 Surface Representation

Surface texture data are represented as  $N_x \times N_y$  pixels digital image, where  $N_x$  and  $N_y$  are the number of pixels in the horizontal and vertical directions, respectively. Let  $L_x = \{1, 2, \dots, N_x\}$ ,  $L_y = \{1, 2, \dots, N_y\}$ , and  $L_z = \{1, 2, \dots, N_z\}$  be spatial domains  $X$ ,  $Y$ , and gray-scale level domain  $Z$ , respectively. Then, the image can be defined as a function  $z = I(x, y)$  which assigns a gray-scale level value  $z \in L_z$  to a pixel located at  $(x, y) \in L_x \times L_y$ , where  $x$  and  $y$  are integer numbers representing coordinates of pixels in  $X$  and  $Y$  domains, and  $N_z$  is the total number of gray-scale level values.

#### 3.1.2 BRG Method

The BRG method is a generalization of the FS analysis (FSA) method into all possible directions [18]. In the FSA method, FDs are calculated in horizontal ( $\theta_1$ ) and vertical ( $\theta_2$ ) directions [23]. For the calculation of FDs, an image is dilated and eroded in horizontal and vertical directions using a line SE of different sizes  $d_m$  ( $m = 1, 2, \dots, N_d$ ,

**Fig. 3** Examples of QQ and log–log plots constructed for **a–d** wear particle surface shown in Fig. 2, **e–h** circularly polarized self-structured surface (Fig. 1a) and **i–l** twofold symmetrical self-structured surface (Fig. 1c)

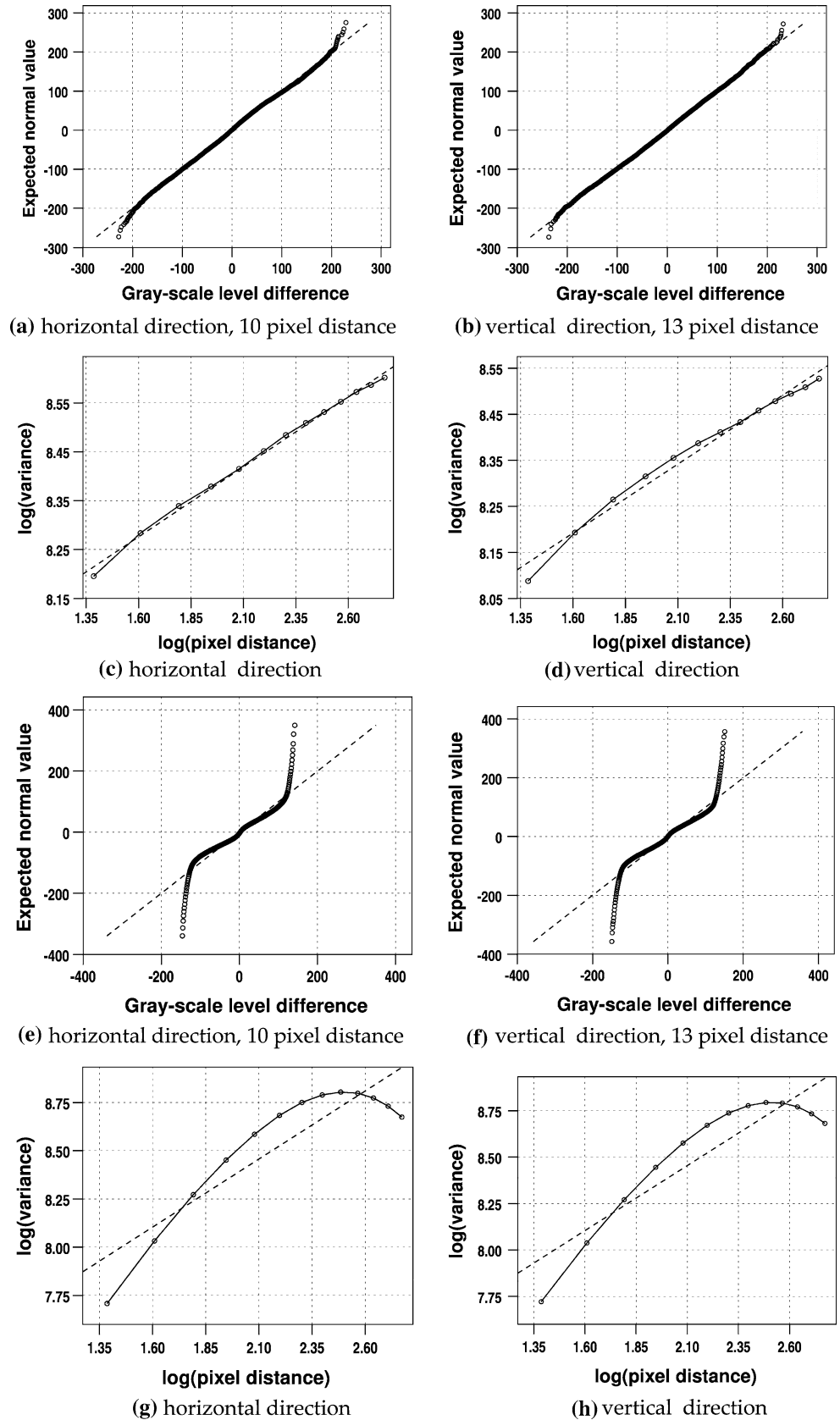
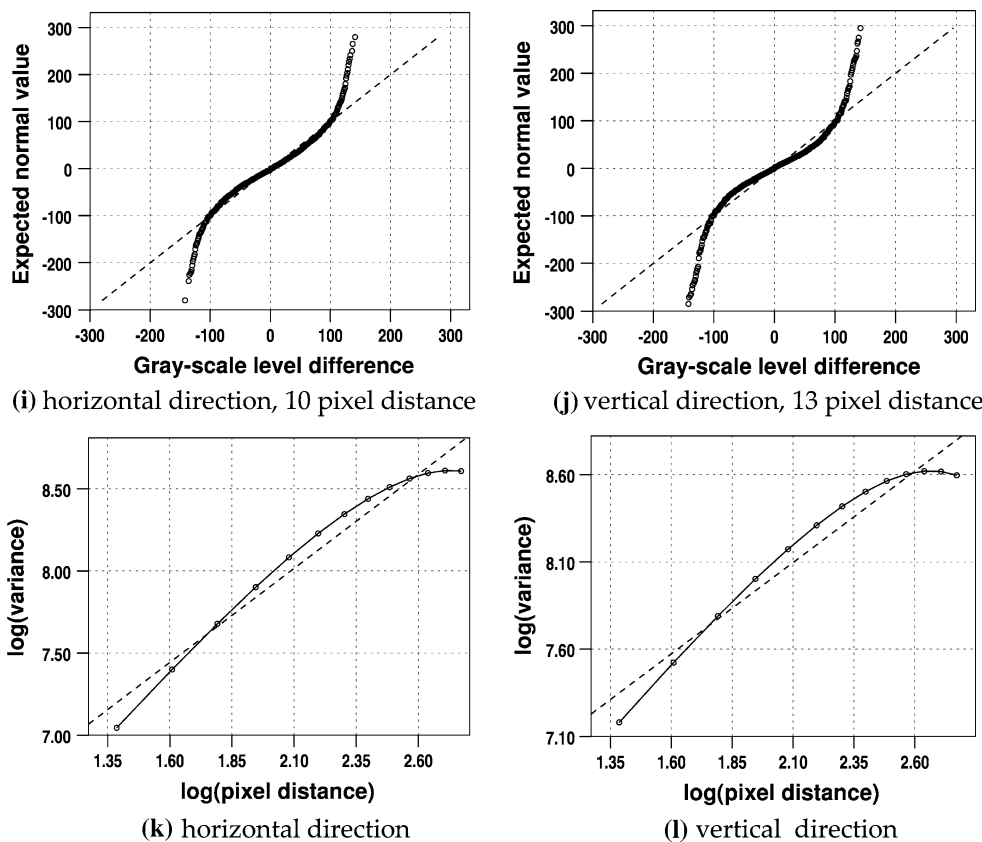


Fig. 3 continued



**Table 1** For each direction  $\theta_n$ , a skewed image is obtained by shearing the original image along its border over calculated distance

$\theta_n$	Image border	Border direction	Border distance
$0^\circ < \theta_n \leq 45^\circ$	Right	Down	$N_y \tan(\theta_n)$
$45^\circ < \theta_n \leq 90^\circ$	Top	Left	$N_x \tan(90^\circ - \theta_n)$
$90^\circ < \theta_n \leq 135^\circ$	Top	Right	$\text{abs}(N_x \tan(90^\circ - \theta_n))$
$135^\circ < \theta_n \leq 180^\circ$	Left	Down	$N_y \tan(180^\circ - \theta_n)$
$180^\circ < \theta_n \leq 225^\circ$	Left	Up	$\text{abs}(N_y \tan(180^\circ - \theta_n))$
$225^\circ < \theta_n \leq 270^\circ$	Bottom	Right	$N_x \tan(\theta_n - 270^\circ)$
$270^\circ < \theta_n \leq 315^\circ$	Bottom	Left	$\text{abs}(N_x \tan(\theta_n - 270^\circ))$
$315^\circ < \theta_n < 360^\circ$	Right	Up	$N_y \tan(360^\circ - \theta_n)$

For  $45^\circ < \theta_n \leq 135^\circ$  and  $225^\circ < \theta_n \leq 315^\circ$  skewed images are rotated clockwise by  $90^\circ$

where  $N_d$  is the total number of sizes); then, surface volumes enclosed between dilated and eroded images are calculated and used to obtain surface areas. The areas are plotted against SE sizes in log–log coordinates. The plot data points are divided into overlapping sets and a line is fitted to each set. FDs are calculated as  $2 - S$ , where  $S$  is a slope of the line fitted at individual scales (the middle point of each set).

Generalization of the FSA method into other directions was made using a square rotating grid. As the grid

rotates around its center over the image by predefined angle  $\theta_n$ , where  $n = 3, 4, \dots, N_\theta$  and  $N_\theta$  is the number of directions, image pixels covered by it are copied into a matrix. Dilated and eroded versions of the matrix are then used to calculate FDs in the same way as in the FSA method. Specifically, the BRG method is performed as follows:

- I. Let  $n = 3$ .
- II. A square grid of  $N_g \times N_g$  pixels, where  $N_g = \text{floor}(\min\{N_x, N_y\}/\sqrt{2})$ , is generated and superimposed on the image. The image and grid are concentric and their borders are parallel.
- III. The grid is rotated by an angle  $\theta_n$  around its center and image pixels covered by the grid are copied into a matrix  $\mathbf{K}_n$  of size  $N_g \times N_g$ . This is performed by the procedure proposed by Geraets [24].
- IV. Let  $m = 2$ .
  1. Dilated and eroded versions of  $\mathbf{K}_n$  are obtained by a horizontal line SE of size  $d_{m-1}$  pixels.
  2. Step 1 is repeated for SE of size  $d_m$  pixels.
  3. Surface area  $A(d_m, \theta_n)$  is calculated as  $\{V(d_m, \theta_n) - V(d_{m-1}, \theta_n)\}/2$ , where  $V(d_m, \theta_n)$  is the volume enclosed between the dilated and eroded  $\mathbf{K}_n$ .
  4. Steps 1 to 3 are repeated for  $m = 3, 4, \dots, N_d$ .
  5. A log–log plot of  $A(d_m, \theta_n)$  against  $d_m$  is constructed.

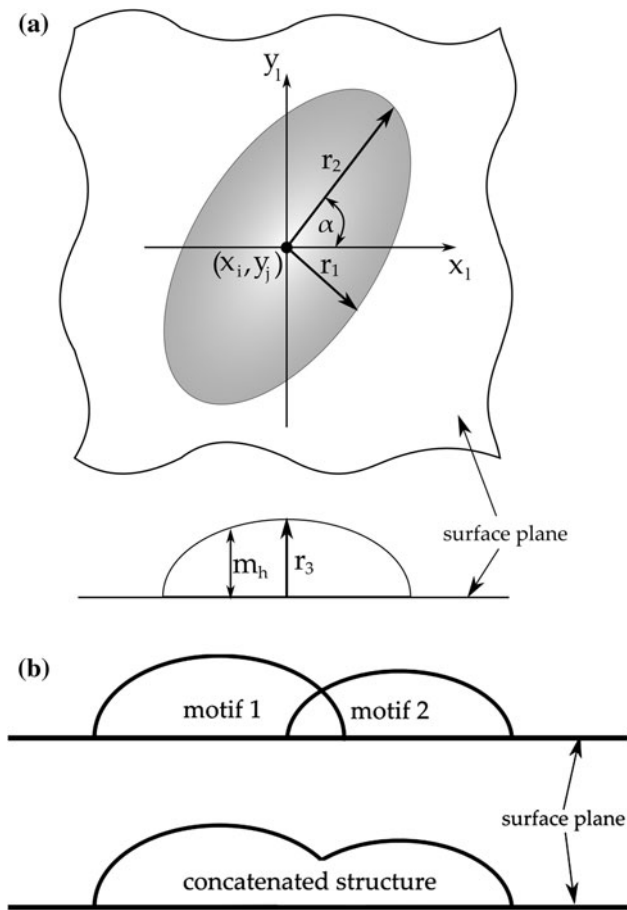


**Fig. 4** Schematic illustrations of **a** a half-ellipsoid motif and **b** a concatenation of two overlapping motifs

6. Log–log data points are divided into the overlapping sets of  $p$  data points, a line is fitted to each set and FDs are calculated.
- V. Steps II to IV are repeated for  $n = 4, 5, \dots, N_\theta$ .

### 3.1.3 ABRG Method

A limitation of the BRG method is that the grid is smaller than the image [18]. Consequently, as the grid rotates, some parts of the image are not covered (e.g., corners of the image). In the ABRG method, this problem was overcome by adjusting the grid and matrix  $\mathbf{K}_n$  (i.e.,  $N_g \times N_h$  pixels) for each direction in such a way that the entire image is covered. For  $0^\circ \leq \theta_n < 90^\circ$  and  $180^\circ \leq \theta_n < 270^\circ$ , the  $N_g$  and  $N_h$  sizes are adjusted as follows:

$$N_g = \text{abs}(\text{floor}(N_x \cos(\theta_n) + N_y \sin(\theta_n))),$$

$$N_h = \text{abs}(\text{floor}(N_x \sin(\theta_n) + N_y \cos(\theta_n))).$$

For other values of  $\theta_n$ , the negative  $\theta_n$  (i.e.,  $-\theta_n$ ) is used. In the vertical and horizontal directions, the grid and image sizes are equal, i.e.,  $N_g = N_x$  and  $N_h = N_y$ .

### 3.1.4 BSI Method

In the BSI method, FDs are calculated in the same way as in the BRG and ABRG methods. However, the rotating grid is not used. Instead, dilations and erosions are performed on skewed versions of the original image. Skewed images are obtained by shearing the original image along its border over calculated distance by means of cubic interpolation (Table 1). Previous studies showed that morphological operations using horizontal SEs on a skewed image as compared to those using interpolated SEs on the original image is a good compromise between accuracy and computational efficiency [25, 26].

## 3.2 Methods Evaluation

### 3.2.1 Motif-Based Texture Generator

A MTG was developed and used to produce texture images of artificial self-structured surfaces. In the generator, a half-

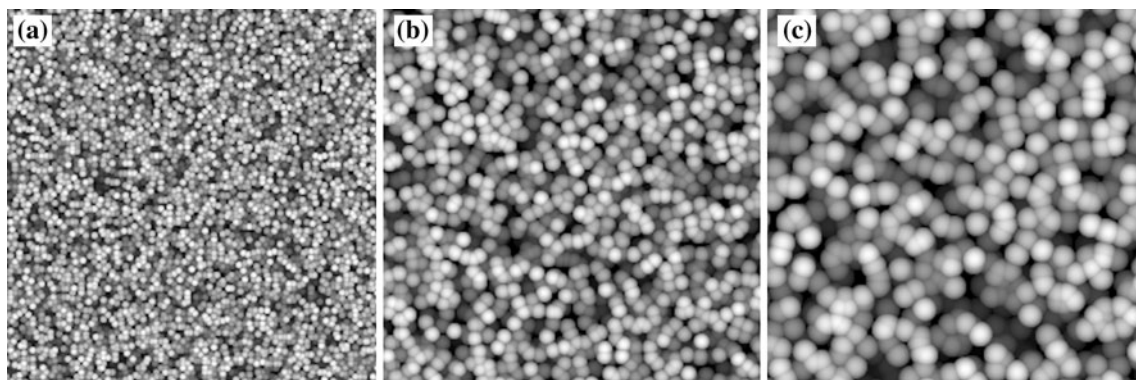


**Fig. 5** Computer-generated isotropic self-structured surface texture images with decreasing roughness.  $R_a$  measured for those surfaces were **a** 0.025  $\mu\text{m}$ , **b** 0.018  $\mu\text{m}$ , and **c** 0.011  $\mu\text{m}$  (cut-off value of 0.8  $\mu\text{m}$ )

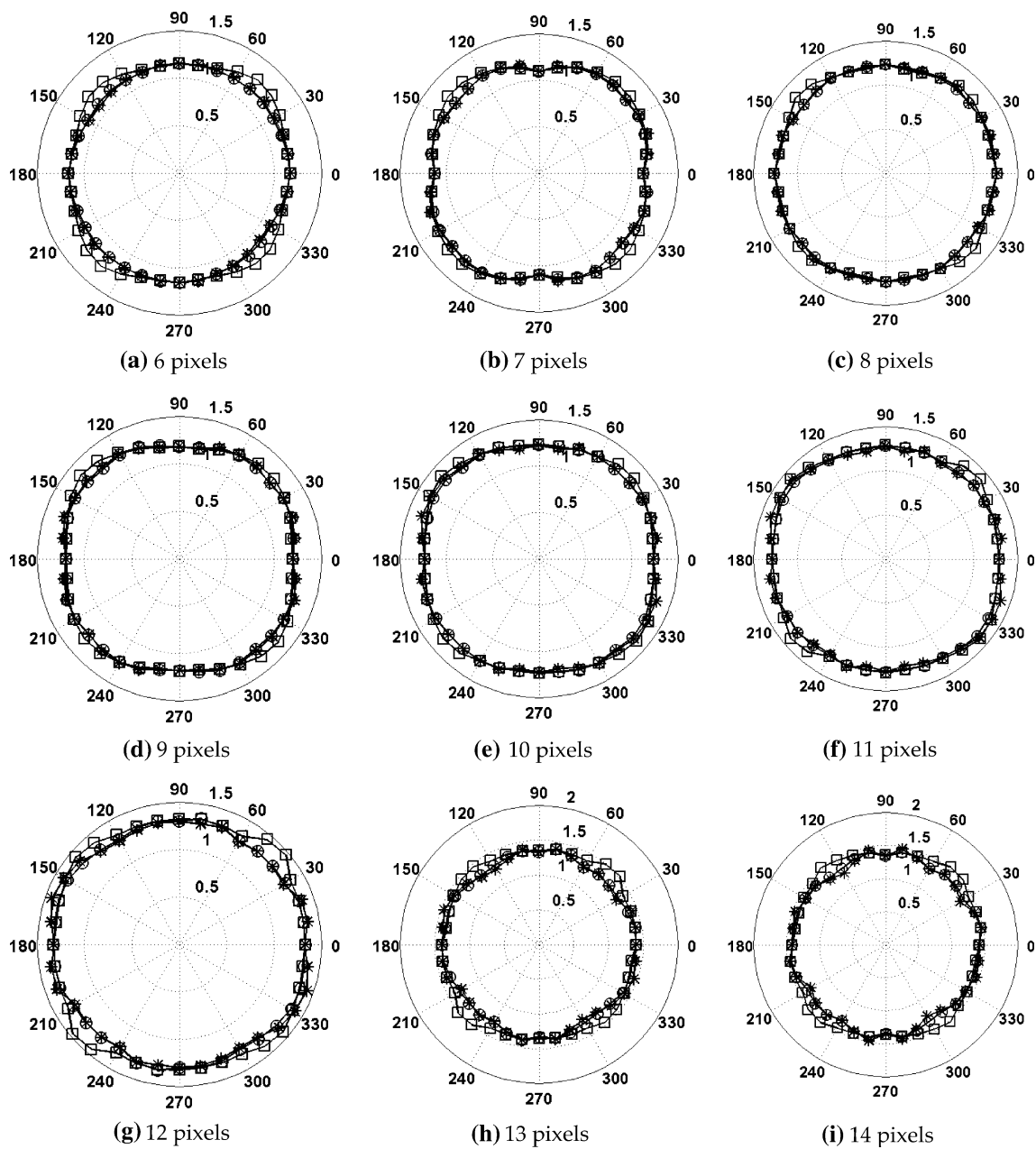


**Fig. 6** Rose plots of slopes at nine scales obtained by means of BRG (*asterisk*), ABRG (*open circle*), and BSI (*open square*) methods for the roughest isotropic self-structured surface (Fig. 5a)

ellipsoid motif (i.e., a recurring surface element) is distributed on an empty image (i.e., all gray-scale level values set to zero) according to the user pre-defined rules. A surface height  $m_h$  of the motif is given by

$$m_h(x_1, y_1) = r_3 \sqrt{1 - \frac{(x_1 \cos \alpha - y_1 \sin \alpha)^2}{r_1^2} - \frac{(x_1 \sin \alpha + y_1 \cos \alpha)^2}{r_2^2}}$$

where  $r_1$ ,  $r_2$ , and  $r_3$  are the ellipsoid radii,  $x_1$  and  $y_1$  are local coordinates with their origin located at the center of the

ellipsoid ( $x_i, x_j$ ), and  $\alpha$  is the orientation measured with respect to the image horizontal axis (Fig. 4a). A self-structured surface texture is built in the following steps:

1. An empty image  $I_r$  of size  $N_r \times N_r$  is generated where  $N_r = \text{floor}(\max\{N_x, N_y\} * \sqrt{2})$ .
2. Let the initial coordinates of centers of motifs be  $x_i = \{i * s_x - N_r/2: i = 0, 1, \dots, N_r/s_x\}$  and  $y_j = \{j * s_y - N_r/2: j = 0, 1, \dots, N_r/s_y\}$ .  $s_x$  and  $s_y$  are given distances between centers. The  $x_i$  and  $y_j$  coordinates are calculated with respect to the center of  $I_r$ .

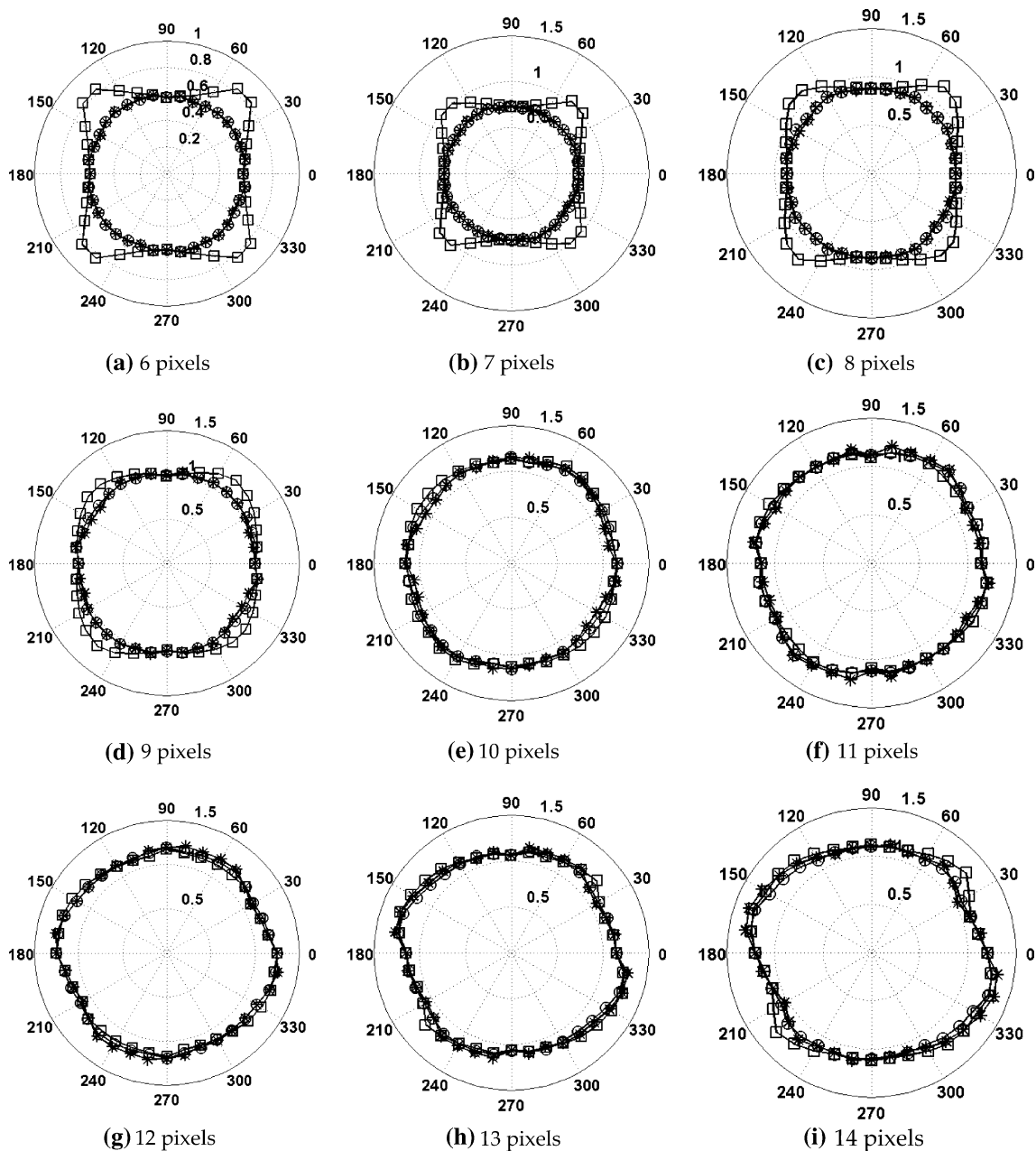


**Fig. 7** Rose plots of slopes at nine scales obtained by means of BRG (*asterisk*), ABRG (*open circle*), and BSI (*open square*) methods for the medium rough isotropic self-structured surface (Fig. 5b)

3. Let  $j = 0$

3.1 Let  $i = 0$

3.2 Coordinates  $x_i$  and  $y_j$  are translated in the horizontal and vertical directions by a random number of pixels, i.e.,  $x' = x_i + a_1 \text{rand}(-s_x, s_x)$  and  $y' = y_j + a_2 \text{rand}(-s_y, s_y)$ . “rand” returns a uniformly distributed pseudo-random number between  $-s_x$  and  $s_x$ , and  $a_1$  and  $a_2$  are scaling factors.

3.3  $x'$  and  $y'$  are rotated around the center of  $I_r$  by a given angle  $\beta$ , i.e.,  $x'' = x' \cos(\beta) - y' \sin(\beta)$  and  $y'' = x' \sin(\beta) + y' \cos(\beta)$ .

3.4  $x''$  and  $y''$  are converted to their corresponding coordinates on  $I_r$ , i.e.,  $x_r = \text{round}(x'' + N_r/2 + 1)$  and  $y_r = \text{round}(y'' + N_r/2 + 1)$  where “round” is a function that rounds a value to the nearest integer.

3.5 The half-ellipsoid motif is located at  $x_r$  and  $y_r$  coordinates on  $I_r$ .



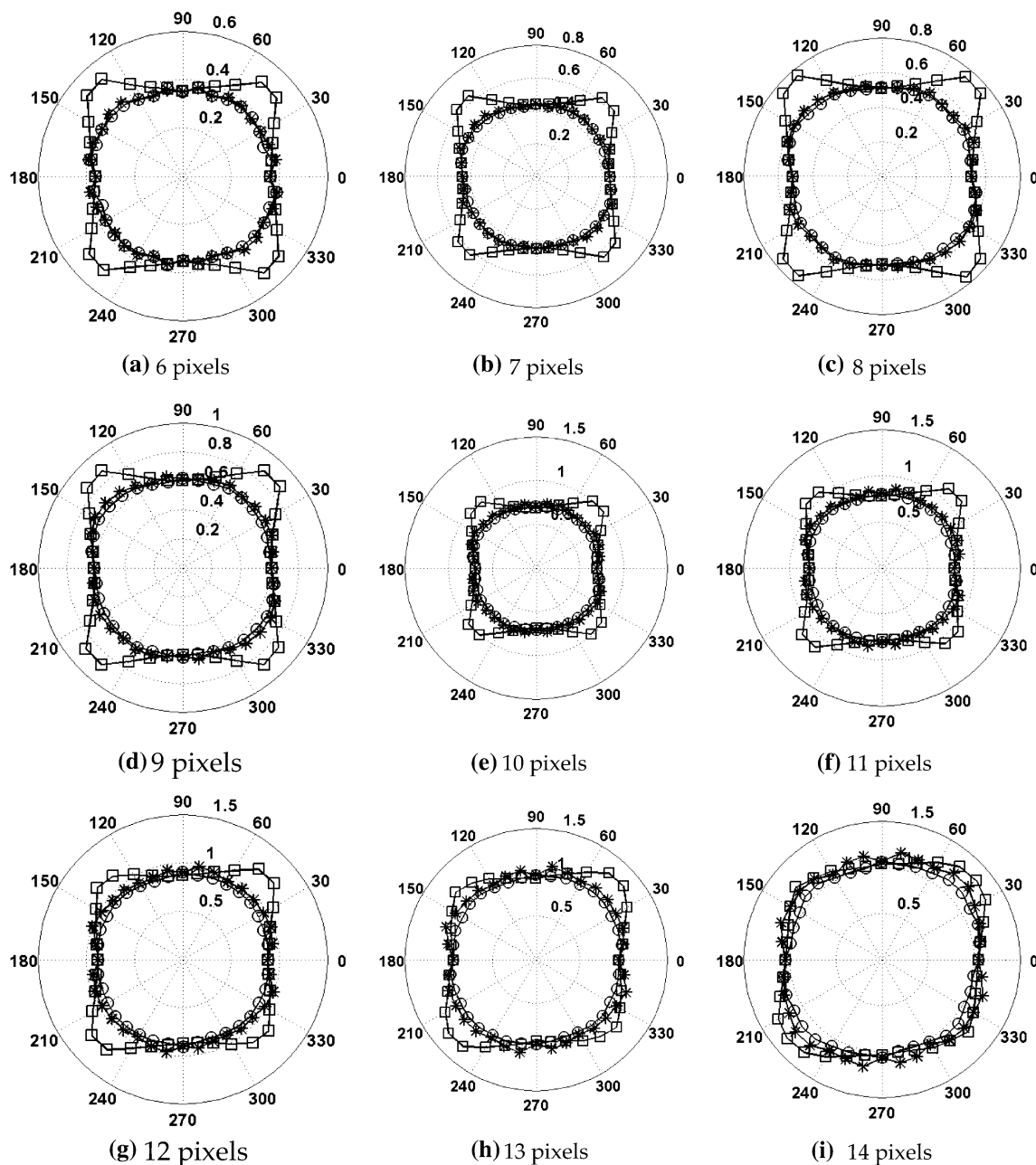


**Fig. 8** Rose plots of slopes at nine scales obtained by means of BRG (*asterisk*), ABRG (*open circle*), and BSI (*open square*) methods for the least rough isotropic self-structured surface (Fig. 5c)

3.6 If there is an overlap between the currently and previously generated motifs, the motifs are concatenated. This is done by taking the maximum values of heights in the image area covered by overlapping motifs (Fig. 4b).

3.7  $i = i + 1$  and go to step 3.2 unless  $i > N_r/s_x$ .

4.  $j = j + 1$  and go to step 3 unless  $j > N_r/s_y$ .

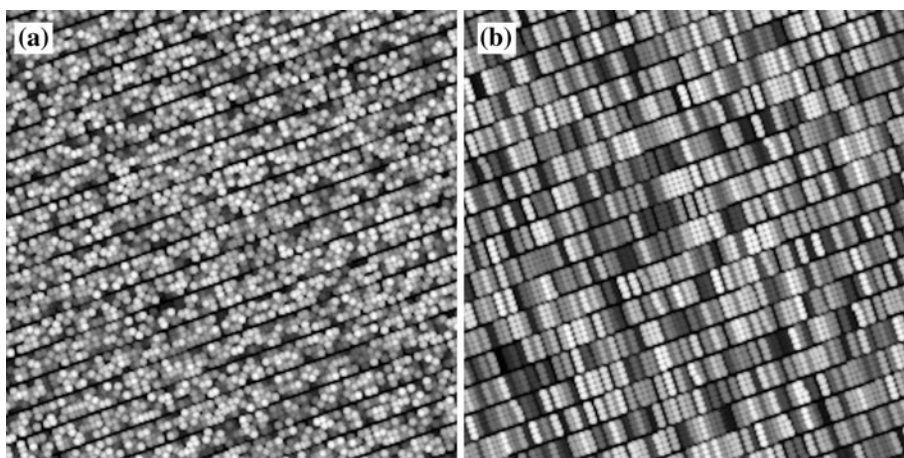
5. The image  $I_r$  is cropped to the size  $N_x \times N_y$  from the pixel with the upper left coordinates  $(x_c, y_c)$  to the pixel with the bottom right coordinates  $(x_c + N_x - 1,$

$y_c + N_y - 1)$ .  $x_c$  and  $y_c$  are defined as  $\text{round}((N_r - N_x)/2)$  and  $\text{round}((N_r - N_y)/2)$ , respectively.

### 3.2.2 Methods Evaluation Setup

The performance of newly developed and BRG methods in measuring surface roughness, directionality, quantifying multi-patterned textures, and detecting differences between textures of self-structured surfaces was evaluated. This evaluation was conducted using images of computer

**Fig. 9** Computer-generated anisotropic self-structured surface texture images with **a** 20° and **b** 20° and 110° dominating directions



generated and real photoinduced self-structured surfaces. All images were not Brownian fractal and had a size of  $256 \times 256$  pixels (for AFM,  $342 \times 342$  pixels) and 256 gray-scale levels. Sizes of SEs used were ranking from 3 to 16 pixels, log–log data points were divided into subsets containing five points and directions were between  $0^\circ$  and  $180^\circ$  in steps of  $10^\circ$ . Nine scales were ranged from 6 to 14 pixels in steps of 1 pixel. Absolute values of slopes  $S$  of lines fitted to log–log plot data points (i.e.,  $S = 2 - \text{FD}$ ) were plotted in polar coordinates as a function of direction. The rose plots were used for visual examination of changes occurring in surface roughness with direction.

## 4 Results

### 4.1 Measurement of Surface Roughness

Three isotropic self-structured surface texture images with decreasing roughness (i.e.,  $R_a = 0.025, 0.018, 0.011 \mu\text{m}$ ; a cut-off value of  $0.8 \mu\text{m}$ ) were generated (Fig. 5).  $R_a$  was calculated for four profiles along the vertical and horizontal directions, assuming the sample size of  $10 \times 10 \mu\text{m}$  and the range of surface heights of  $0.2 \mu\text{m}$ . Similar sizes and ranges can be found for real self-structured surfaces [13]. In MTG,  $r_1 = r_2 = s_x = s_y$  were set to 3, 6, and 9 pixels,  $a_1 = a_2 = 1$ ,  $r_3$  was set individually for each motif as a random integer number between 0 and 256, and  $\beta$  was equal to  $0^\circ$ .

Mean  $\pm$  standard deviation (SD) values of FDs calculated for each image were: for the BRG method,  $3.285 \pm 0.084$ ,  $3.004 \pm 0.212$ , and  $2.749 \pm 0.250$ ; for the ABRG method,  $3.271 \pm 0.079$ ,  $3.003 \pm 0.206$ , and  $2.718 \pm 0.227$ ; and for the BSI method,  $3.295 \pm 0.095$ ,  $3.041 \pm 0.219$ , and  $2.774 \pm 0.250$ . These results show that FDs obtained decrease monotonically with  $R_a$ . The ABRG method had the smallest values of SD, indicating that this

method exhibits less variations between individual FDs than other methods.

Rose plots obtained for each surfaces are shown in Figs. 6, 7, and 8. For the BRG and ABRG methods, they approximate a circle at all scales showing that the surface roughness (i.e., FDs) does not change significantly with direction (Figs. 6, 7, 8). In contrast, the plots obtained for the BSI method deviate from the circular shape. Specifically, at scales between 6 and 8 pixels (Fig. 7), the medium rough surface has the highest FDs in around  $45^\circ$  and  $135^\circ$  directions. Similar results were obtained for the roughest surface at scales from 6 to 13 pixels (Fig. 8).

These findings indicate that ABRG is the best performing in measuring surface roughness.

### 4.2 Measurement of Surface Directionality

The accuracy of the DFS methods in measuring surface directions was evaluated using two anisotropic self-structured surface texture images (Fig. 9). The surface (Fig. 9a) was generated using  $\beta = 20^\circ$ ,  $r_1 = r_2 = s_x = s_y = 3$ ,  $a_1 = a_2 = 0$ . For each motif,  $r_3$  was set individually as a random integer number between 0 and 256. Every fifth row of initial center coordinates of motifs was deleted (i.e.,  $j/5 = 0$ ). The dominating direction of the surface is  $20^\circ$ . The second surface (Fig. 9b) had  $20^\circ$  and  $110^\circ$  dominating directions and it was generated by means of the same parameters as the first one, except that  $r_3$  was selected randomly for groups of four motifs.

Figure 10 shows rose plots of slopes obtained by means of BRG and ABRG methods for the anisotropic self-structured surface with one dominating direction. They approximate a circle at scales from 6 to 12 pixels and they show rapid changes in texture roughness at 13 and 14 pixel scales. The highest roughness was in  $110^\circ$  direction. The BSI method produced similar results except that the rose plots were circular at scales from 6 to 9 pixels. For the

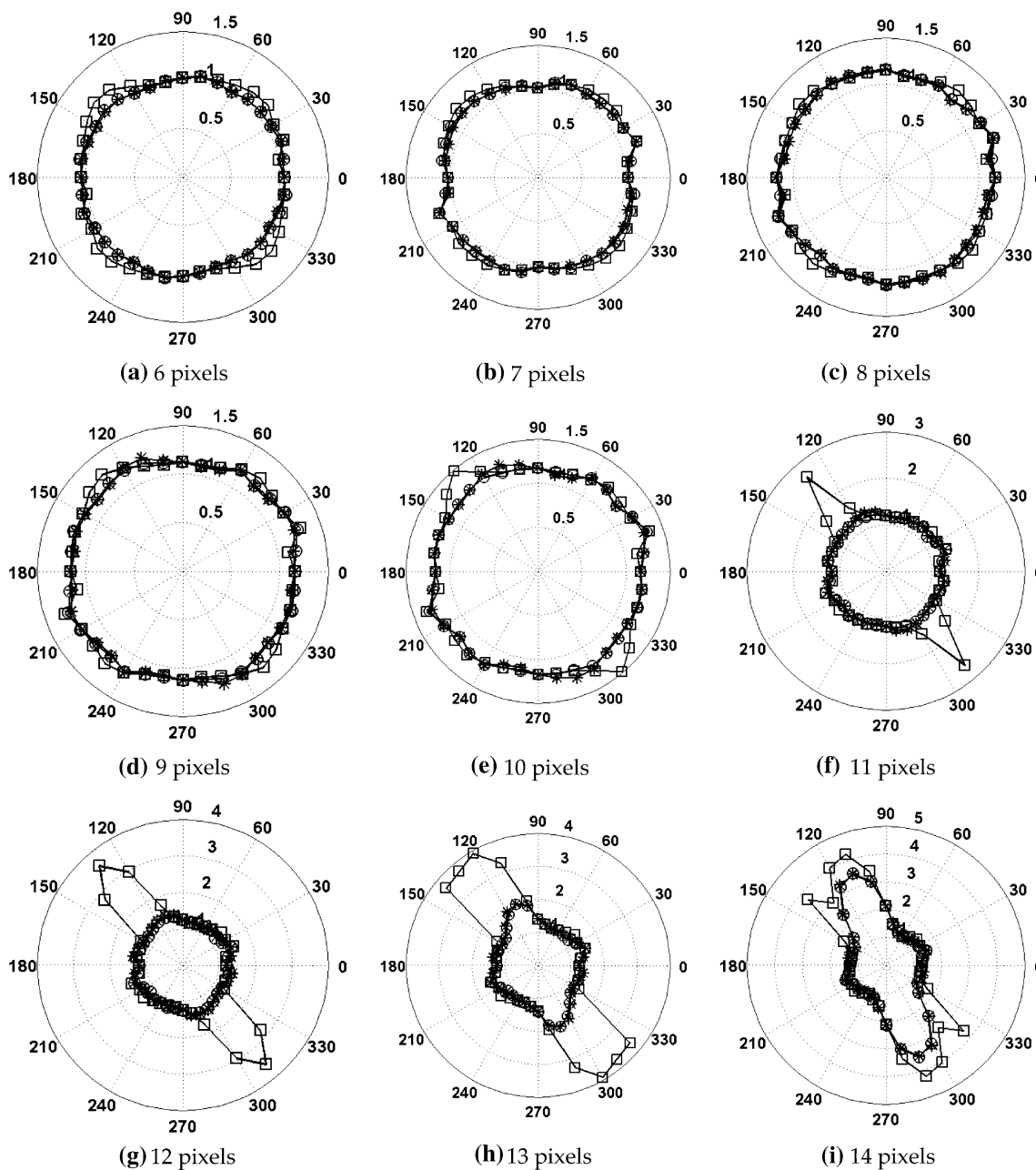


**Fig. 10** Rose plots of slopes at nine scales obtained by means of BRG (*asterisk*), ABRG (*open circle*), and BSI (*open square*) methods for anisotropic self-structured surface with dominating direction of 20° (Fig. 9a)

anisotropic surface with two dominating directions, the BRG and ABRG methods show visible changes in roughness at scales from 6 to 12 pixels (Fig. 11) with the highest and lowest values of slopes in 20° and 110° directions, respectively. At a scale of 14 pixels, slope values do not change considerably with direction except those calculated between 90° and 140°. For the BSI method, slopes took the highest and lowest values in 90° and 110° directions at scales from 6 to 10 pixels. For the remaining scales, the slopes were highest around 120° direction. In other directions, slope values are virtually constant.

The above results show that the BRG and ABRG methods are most accurate in measuring surface directions.

### 4.3 Capacity for Quantifying Multi-patterned Textures

The methods were used to quantify multi-patterned textures using two images of self-structured surface textures with two patterns (Fig. 12). The first surface (Fig. 12a) is isotropic; it has sparsely distributed small motifs along the top border, and densely distributed large motifs elsewhere. Parameters  $r_1 = r_2 = s_x = s_y$  were set to 6 pixels and

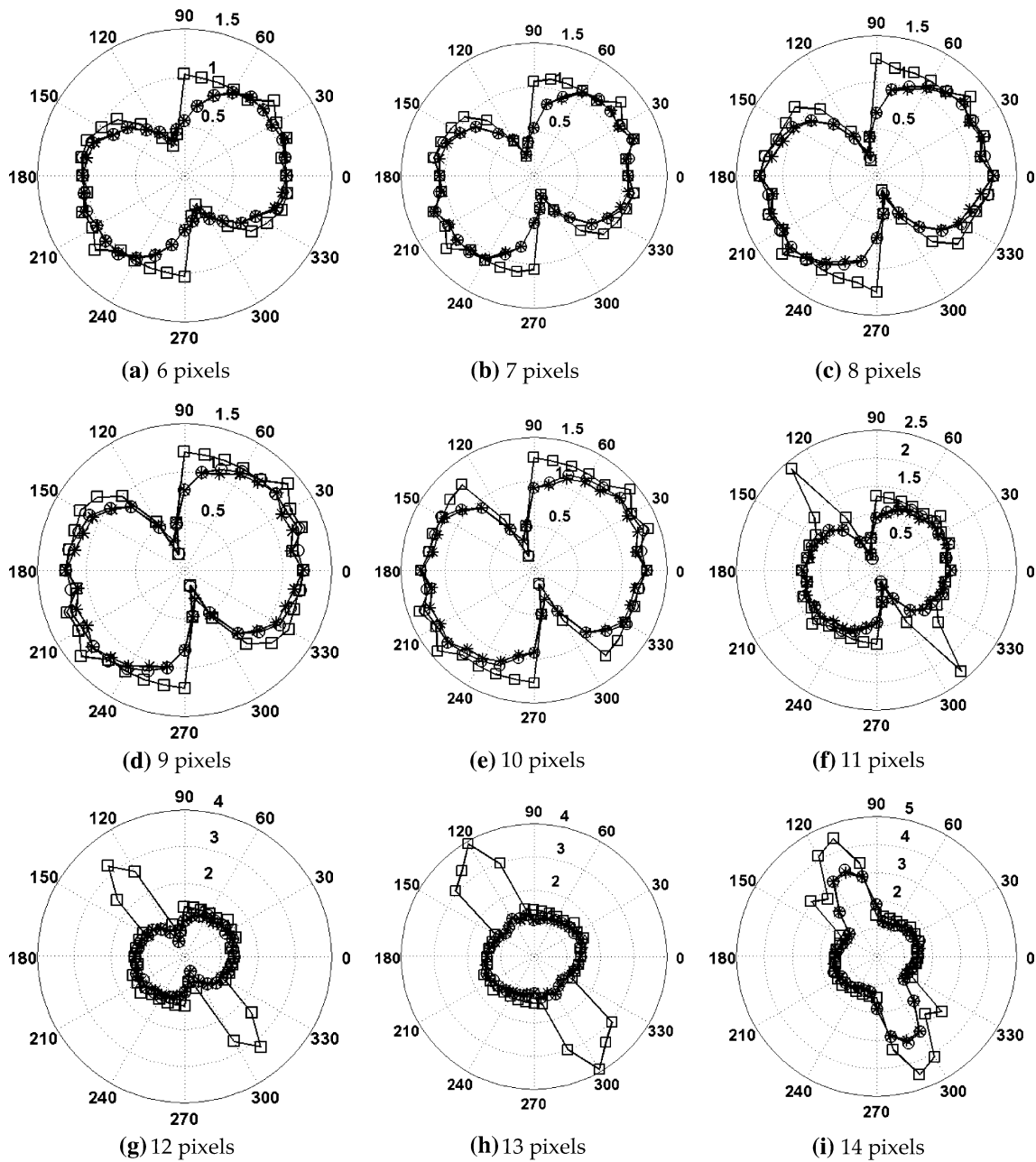


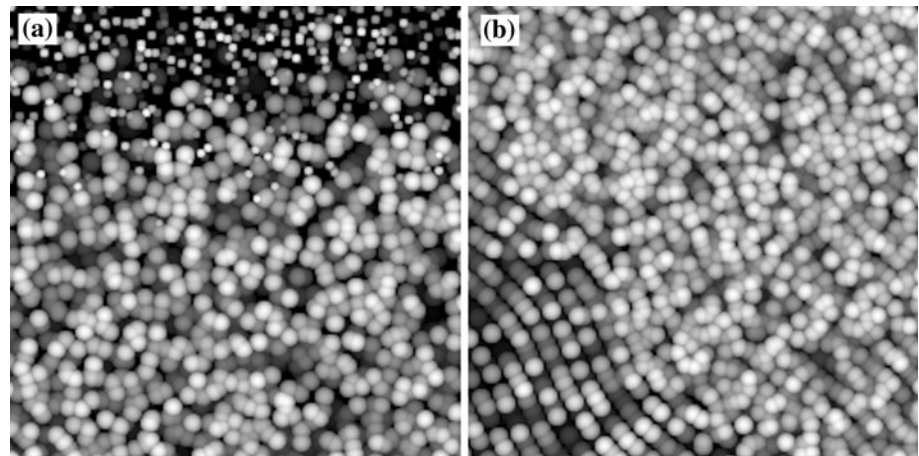
**Fig. 11** Rose plots of slopes at nine scales obtained by means of BRG (asterisk), ABRG (open circle), and BSI (open square) methods for anisotropic self-structured surface with dominating directions of  $20^\circ$  and  $110^\circ$  (Fig. 9b)

$a_1 = a_2$  to 1 pixel.  $r_3$  was set individually for each motif as a random integer number between 0 and 256, and  $\beta$  was  $0^\circ$ . Motifs with  $j$  less than  $45 + \text{rand}(0,10)$  had  $r_1 = r_2 = 3$  pixels. The second surface (Fig. 12b) has densely distributed large motifs except the left-bottom part where the motifs are distributed along sine-shaped curves. This surface is partially isotropic, i.e., only the left-bottom part exhibits some directionality. The surface was generated with the parameter setting used before, except that

$\beta = 130^\circ$  and for  $j$  less than  $45 + \text{rand}(0,10)$ ,  $a_1 = a_2 = 0$ ,  $s_y = 12$  pixels, and  $y' = y_j + 8\sin(4\pi x'/N_x)$ .

Rose plots obtained for the isotropic multi-patterned surface using the ABRG have circular shape at all scales (Fig. 13). Rose plots constructed for the BRG method have small spikes in the vertical direction at scales from 6 to 10 pixels and intrusions in directions between  $60^\circ$  and  $90^\circ$  at other scales. For the BSI method, they have circular shape at scales from 11 to 14 pixels, approximately a

**Fig. 12** Computer-generated **a** isotropic and **b** partially isotropic multi-patterned self-structured surface texture images



square at scales 6–10 pixels and the highest FDs along  $45^\circ$  and  $135^\circ$ . For the partially isotropic surface, the BRG and ABRG methods gave rose plots of a circular shape at scales from 6 to 9 pixels, an elliptical shape at scales from 10 to 12 pixels, and a rectangular shape in the last two scales (Fig. 14). The results obtained for the BSI method are similar except that at scales from 6 to 9 pixels rose plots have a square shape, indicating that roughness is highest in  $45^\circ$  and  $135^\circ$ .

From these results, it appears that the ABRG method performs better in quantifying multi-patterned self-structured surfaces textures than other methods.

#### 4.4 Detection of Differences Between Self-Structured Surface Textures

The ability of the methods to detect differences between self-structured surface textures was evaluated using two AFM images of photoinduced self-structured surfaces (Fig. 1a, b). Specifically, the surfaces were obtained by irradiation of an azo polymer film (Tr-AZ-CN) with circularly (Fig. 1a) and linearly (Fig. 1b) polarized laser beams [13]. For each surface, the thickness of the Tr-AZ-CN films was 250 nm, the intensity of the laser beam was  $200 \text{ mW/cm}^2$ , and the irradiation time was 15 min.

Rose plots of slopes constructed for the BRG and ABRG methods show that the roughness of circularly polarized surface does not change considerably with directions at scales from 6 to 14 pixels (Fig. 15). For the linearly polarized surface (Fig. 1b), the plots show rapid changes in roughness with directions at all scales; the highest roughness is between  $120^\circ$  and  $150^\circ$ , and the lowest roughness is around  $90^\circ$  direction (Fig. 16). For the BSI method, rose plots show that both surfaces exhibit similar cross-shaped changes in roughness. The cross has  $45^\circ$  and  $135^\circ$  directions at all scales for the first surface and at scales from 6 to 11 pixels for the second surfaces. At other scales, the BSI

method produces highest roughness in directions between  $120^\circ$  and  $180^\circ$ ; the lowest roughness between  $45^\circ$  and  $90^\circ$ .

These results indicate the BRG and ABRG method detected more differences between the two self-structured surfaces that the BSI method does.

## 5 Discussion

In this work, two new DFS methods, called ABRG and BSI, were developed for the characterization of self-structured surface textures and compared to the BRG method. Unlike other methods, the new methods do not require image data to be Brownian fractal and use the entire image data in calculations. In the ABRG method, this was achieved through the rotating grid that is automatically adjusted for each direction; in the BSI method, through shearing the original image along its border over calculated distance. For the evaluation of the methods, a special generator, called MTG, was developed to produce artificial texture images of self-structured surfaces. Real self-structured surfaces generated with differently polarized laser beams were also used in the analysis.

The performance of the methods in measuring surface roughness was evaluated using isotropic self-structured surfaces with decreasing roughness. Results obtained showed that the BRG and BSI methods gave the worst performance. This can be attributed to the fact that the rotating grid in BRG is smaller than the image, and subsequently, as the grid rotates image data at the corners are not used. Isotropic self-structured surfaces were visually compared to their skewed versions at  $45^\circ$  and  $135^\circ$ . It was observed that the shape of motifs changed from spherical to elliptical with the major axis oriented in  $45^\circ$  direction. This indicates that image shearing changes surface texture. Because of the changes introduced to texture, BSI method is excluded from further discussion.

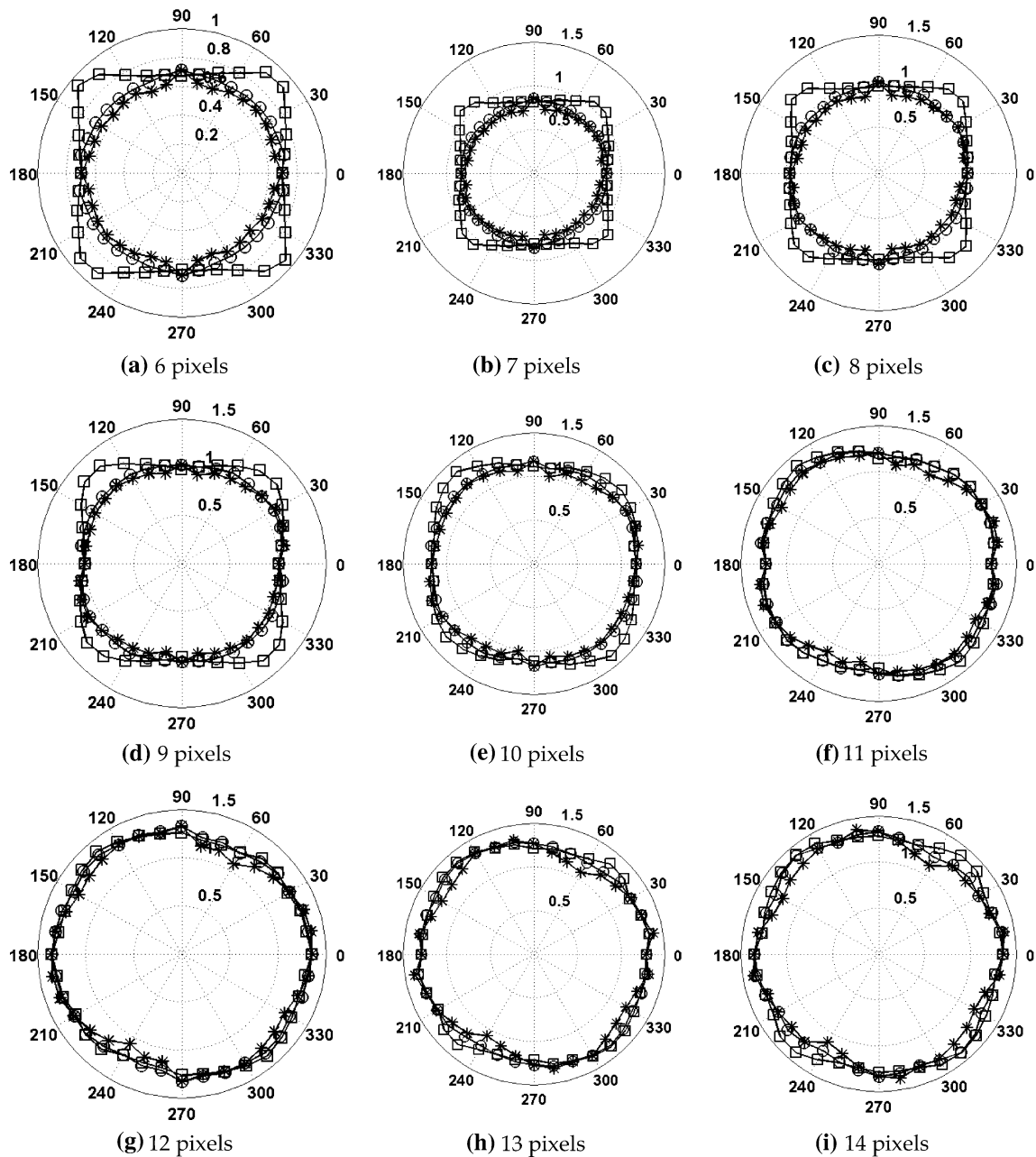


**Fig. 13** Rose plots of slopes at nine scales obtained by means of BRG (*asterisk*), ABRG (*open circle*), and BSI (*open square*) methods for isotropic multi-patterned self-structured surface (Fig. 12a)

The accuracy of the ABRG and BRG methods in measuring surface directionality was investigated. For this purpose, anisotropic self-structured surfaces with known directions were generated. The BRG and ABRG methods produced similar results, i.e., the surface with one dominating direction is approximately isotropic at scales from 6 to 12 pixels and anisotropic at 13 and 14 pixels. This agrees with visual assessment. The surface exhibits stripes with 13–15 pixel width that are oriented in  $20^\circ$  direction; within the stripes, motifs do not have directions.

Consequently, FDs calculated at scales smaller than the line widths (i.e., from 6 to 12 pixels) do not change with direction, and at larger scales (i.e., the widths of stripes) have the largest values in  $110^\circ$  direction. For the surface with two dominating directions, the methods showed changes in roughness at all scales.

Capability of the methods for quantifying multi-patterned textures was investigated using generated isotropic and partially isotropic multi-patterned self-structured surfaces. It was found that the ABRG method performs better

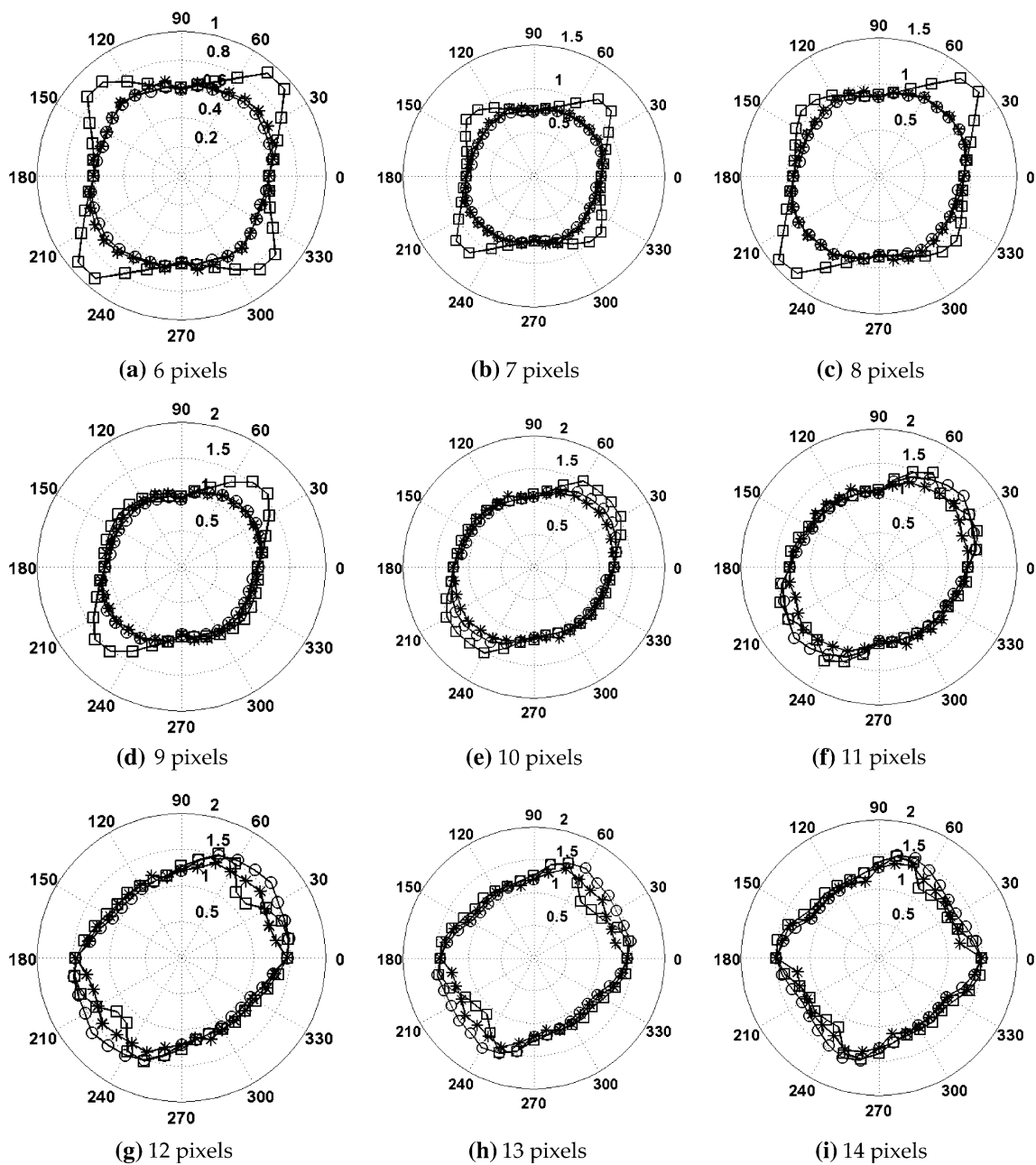


**Fig. 14** Rose plots of slopes at nine scales obtained by means of BRG (*asterisk*), ABRG (*open circle*), and BSI (*open square*) methods for partially isotropic multi-patterned self-structured surface (Fig. 12b)

than the BRG method. The ABRG method correctly quantified that at all scales the roughness of the isotropic multi-pattern surface does not change with direction. The BRG method showed that the surface has the highest roughness in vertical direction. The reason is that the image data is not fully covered by the rotating grid. Consequently, FDs do not quantify the entire multi-patterned textures.

Ability of the methods to detect differences between real self-structured surface textures was evaluated. AFM images of surfaces obtained using circularly and linearly polarized laser beams were used. BRG and ABRG methods

gave similar results, i.e., the circularly and linearly polarized surfaces are isotropic and anisotropic, respectively. This agrees with visual examination. The first surface consists of spherically shaped motifs that have similar sizes and are almost uniformly distributed on a surface. The second surface has ellipsoidal or linearly shaped motifs of different lengths and orientations.

The results obtained in this study demonstrate that the ABRG method has a potential to become useful in characterization of self-structured surface textures. Further evaluation will be undertaken. Especially, our future work

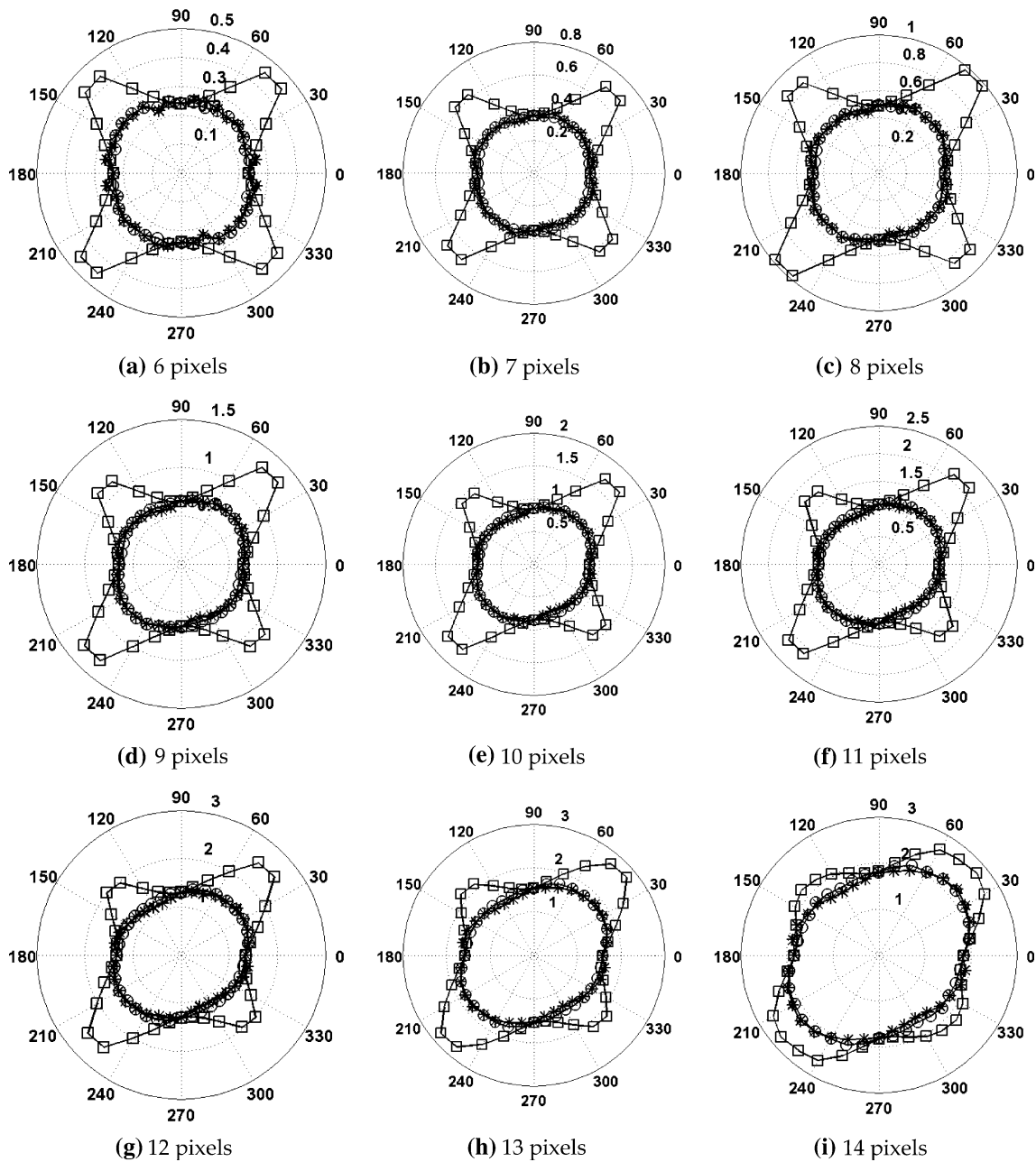


**Fig. 15** Rose plots of slopes at nine scales obtained by means of BRG (*asterisk*), ABRG (*open circle*), and BSI (*open square*) methods for circularly polarized self-structured surface (Fig. 1a)

will focus on studying the effects of AFM imaging conditions on the accuracy of the ABRG method. AFM will be used since it is the most common imaging technique employed for the visualization of self-structured surfaces. Quality of AFM images depends on a number of factors, e.g., imaging modes and force and probe geometry [18, 27, 28]. Also, the ABRG method will be used to study relationship between self-structured surfaces and friction. Currently, there is ongoing research aimed at understanding this relationship [1, 15]. Bhushan et al. [1] performed a correlation analysis between roughness and friction force,

and results obtained were not conclusive. This could be because the surface roughness was evaluated by means of the RMS parameter, which works well only with isotropic surfaces at a single scale.

## 6 Conclusions

From the work conducted in this paper, the following conclusions can be drawn:



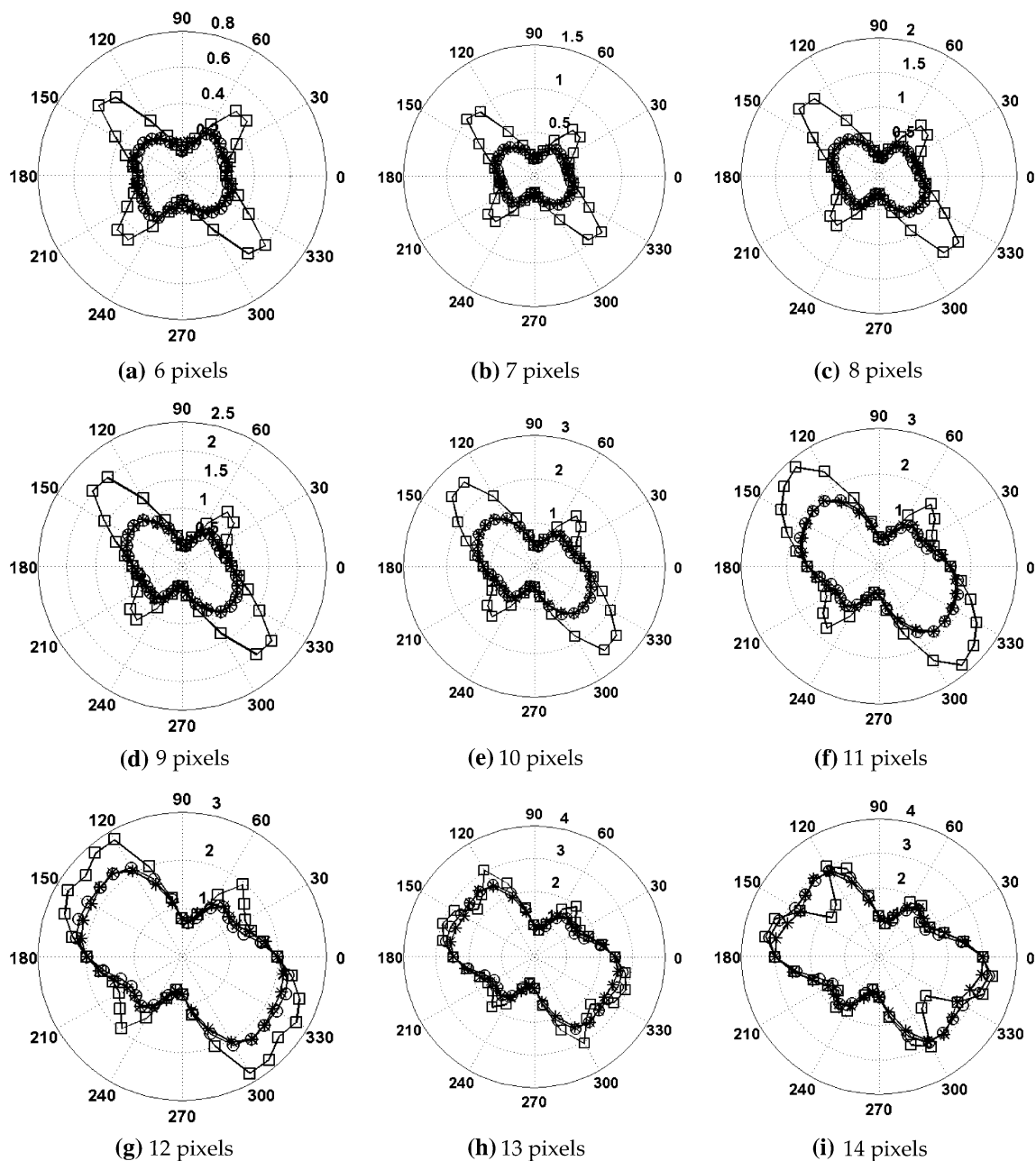


**Fig. 16** Rose plots of slopes at nine scales obtained by means of BRG (*asterisk*), ABRG (*open circle*), and BSI (*open square*) methods for linearly polarized self-structured surface (Fig. 1b)

- Two new methods were developed, i.e., ARBG and BSI methods, for the characterization of self-structured surfaces at different scales and directions. The methods calculate FDs at individual scales in different directions and they do not require surface textures to be Brownian fractal.
- The performance of the new methods and the BRG method was evaluated using computer generated images of artificial self-structured surface textures and AFM images of real self-structured surfaces. For the generation of computer images, a MTG was developed.
- The accuracy of the methods in measuring surface roughness and directionality and their capacity for quantifying multi-patterned textures were investigated. The ABRG method was the best performing.
- In detection of differences between textures of real self-structured surfaces produced by circularly and linearly polarized laser beams, the BRG and ABRG methods were most sensitive.

**Acknowledgments** The authors wish to thank the University of Western Australia and the School of Mechanical and Chemical Engineering for their support during preparation of the manuscript.

**Conflict of interest** The authors have no conflict of interest for this manuscript.

## References

- Bhushan, B., Kulkarni, A.V., Koinkar, V.N.: Microtribological characterization of self-assembled and Langmuir-Blodgett monolayers by atomic and friction force microscopy. *Langmuir* **11**, 3189–3198 (1995)
- Nakano, M.: Tribological properties of self-assembled monolayers. In: Biresaw, G. (ed.) *Surfactants in Tribology*, vol. 2, pp. 3–15. CRC Press, Boca Raton (2011)
- Wang, Y., Mo, Y.F., Zhu, M., Bai, M.W.: Wettability and nanotribological property of multiply alkylated cyclopentanes (MACs) on silicon substrates. *Tribol. Trans.* **53**(2), 219–223 (2010)
- Hurst, K.M., Ansari, N., Roberts, C.B., Ashurst, W.R.: Self-assembled monolayer-immobilized gold nanoparticles as durable, anti-stiction coatings for MEMS. *J. Microelectromech. Syst.* **20**, 424–435 (2011)
- Bishop, A.R., Nuzzo, R.G.: Self-assembled monolayers: recent developments and applications. *Curr. Opin. Colloid Interface Sci.* **1**, 127–136 (1996)
- Chaki, N.K., Vijayamohan, K.: Self-assembled monolayers as a tunable platform for biosensor applications. *Biosens. Bioelectron.* **17**, 1–12 (2002)
- Tsukruk, V.V.: Molecular lubricants and glues for micro- and nanodevices. *Adv. Mater.* **13**(2), 95–108 (2001)
- Love, J.C., Estroff, L.A., Kriebel, J.K., Nuzzo, R.G., Whitesides, G.M.: Self-assembled monolayers of thiolates on metals as a form of nanotechnology. *Chem. Rev.* **105**(4), 1103–1169 (2005)
- Kaufmann, C., Mani, G., Marton, D., Johnson, D., Agrawal, C.M.: Long-term stability of self-assembled monolayers on electropolished L605 cobalt chromium alloy for stent applications. *J. Biomed. Mater. Res. B* **98**(2), 280–289 (2011)
- Kudernac, T., Shabelina, N., Mamdouh, W., Hoger, S., De Feyter, S.: STM visualisation of counterions and the effect of charges on self-assembled monolayers of macrocycles. *Beilstein J. Nanotechnol.* **2**, 674–680 (2011)
- Miyake, K., Hori, Y., Ikeda, T., Asakawa, M., Shimizu, T., Sasaki, S.: Alkyl chain length dependence of the self-organized structure of alkyl-substituted phthalocyanines. *Langmuir* **24**(9), 4708–4714 (2008)
- Miyake, K., Fukuta, M., Asakawa, M., Hori, Y., Ikeda, T., Shimizu, T.: Molecular motion of surface-immobilized double-decker phthalocyanine complexes. *J. Am. Chem. Soc.* **131**(49), 17808–17813 (2009)
- Yin, J.J., Ye, G., Wang, X.G.: Self-structured surface patterns on molecular azo glass films induced by laser light irradiation. *Langmuir* **26**(9), 6755–6761 (2010)
- Wang, X.L., Yin, J.J., Wang, X.G.: Photoinduced self-structured surface pattern on a molecular azo glass film: structure-property relationship and wavelength correlation. *Langmuir* **27**(20), 12666–12676 (2011)
- Miyake, K.: Frictional properties of physisorbed layers of self-organized molecules at solid-liquid interface. In: Biresaw, G. (ed.) *Surfactants in Tribology*, vol. 2, pp. 85–101. CRC Press, Boca Raton (2011)
- Lam, K.T., Ji, L.W.: Fractal analysis of InGaN self-assembled quantum dots grown by MOCVD. *Microelectron. J.* **38**(8–9), 905–909 (2007)
- Consolin, N., Leite, F.L., Carvalho, E.R., Venancio, E.C., Vaz, C.M.R., Mattoso, L.H.C.: Study of poly(o-ethoxyaniline) interactions with herbicides and evaluation of conductive polymer potential used in electrochemical sensors. *J. Brazil. Chem. Soc.* **18**(3), 577–584 (2007)
- Wolski, M., Podsiadlo, P., Stachowiak, G.W.: Directional fractal signature analysis of trabecular bone: evaluation of different methods to detect early osteoarthritis in knee radiographs. *Proc. Inst. Mech. Eng. H* **223**(2), 211–236 (2009)
- Wolski, M., Podsiadlo, P., Stachowiak, G.W., Lohmander, L.S., Englund, M.: Differences in trabecular bone texture between knees with and without radiographic osteoarthritis detected by directional fractal signature method. *Osteoarthritis Cartilage* **18**, 684–690 (2010)
- Wolski, M., Stachowiak, G.W., Dempsey, A.R., Mills, P.M., Cicuttini, F.M., Wang, Y., Stoffel, K.K., Lloyd, D.G., Podsiadlo, P.: Trabecular bone texture detected by plain radiography and variance orientation transform method is different between knees with and without cartilage defects. *J. Orthop. Res.* **29**(8), 1161–1167 (2011)
- Wolski, M., Podsiadlo, P., Stachowiak, G.W.: Applications of the variance orientation transform method to the multiscale characterization of surface roughness and anisotropy. *Tribol. Int.* **43**, 2203–2215 (2010)
- Pentland, A.: Fractal-based description of natural scenes. *IEEE Trans. Pattern Anal. Mach. Intell.* **6**(6), 661–674 (1984)
- Lynch, J.A., Hawkes, D.J., Buckland-Wright, J.C.: Analysis of texture in macroradiographs of osteoarthritic knees using the fractal signature. *Phys. Med. Biol.* **36**(6), 709–722 (1991)
- Geraets, W.G.M.: Comparison of two methods for measuring orientation. *Bone* **23**(4), 383–388 (1998)
- Hendriks, C.L.L., van Vliet, L.J.: *Discrete Morphology with Line Structuring Elements. Lecture Notes in Computer Science*, vol. 2756, pp. 1611–3349 (2003)
- Hendriks, C.L.L., van Vliet, L.J.: Using line segments as structuring elements for sampling-invariant measurements. *IEEE Trans. Pattern Anal. Mach. Intell.* **27**(11), 1826–1831 (2005)
- Dufrene, Y.F.: Atomic force microscopy, a powerful tool in microbiology. *J. Bacteriol.* **19**, 5205–5213 (2002)
- Cidade, G.A.G., Anteneodo, C., Roberty, N.C., Neto, A.J.S.: A generalized approach for atomic force microscopy image restoration with Bregman distances as Tikhonov regularization terms. In: *Inverse Problems in Engineering: Theory and Practice 3rd International Conference on Inverse Problems in Engineering*, Port Ludlow, WA, USA, 13–18 June 1999